

# Velocity map imaging study of OCS photodissociation followed by S(<sup>1</sup>S) autoionization at 157 nm

SHIOU-MIN WU<sup>†</sup>, XUEMING YANG<sup>‡</sup> and DAVID H. PARKER<sup>†\*</sup>

<sup>†</sup>Department of Molecular and Laser Physics, Institute for Molecules and Materials, Radboud University Nijmegen, PO Box 9010, NL-6500 GL Nijmegen, The Netherlands

<sup>‡</sup>State Key Laboratory of Molecular Reaction Dynamics, Dalian Institute of Chemical Physics, Chinese Academy of Sciences, Dalian, Liaoning 116023, People's Republic of China

(Received 20 December 2004; in final form 13 January 2005)

Atomic sulphur ions (S<sup>+</sup>) were observed directly by crossing a carbonyl sulphide (OCS) molecular beam with a F<sub>2</sub> laser. In this study both S<sup>+</sup> ion and electron images were measured using the velocity map imaging technique. The results imply that S<sup>+</sup> is produced from the well-known photodissociation of OCS at 157 nm leading to the dominant S(<sup>1</sup>S) + CO(<sup>1</sup>Σ<sup>+</sup>) channel, and then the excited S(<sup>1</sup>S) atom is directly ionized by another 157 nm photon. Correlated vibrationally resolved angular distributions and internal energy distribution of the CO coproducts are reported here and compared with previous studies. This experiment yields strong and sharp S<sup>+</sup> images which may be useful for calibrating any imaging or laser ionization apparatus when using a 157 nm laser. A number of technical aspects such as corrections for partial slicing and imperfect laser polarization are described. Abstraction of product angular distributions using both polarized and unpolarized photolysis lasers is also demonstrated using velocity map imaging.

## 1. Introduction

Professor John Simons and co-workers have shown that vector properties such as product angular momentum polarization reveal many intricate aspects of molecular photodissociation dynamics [1]. In a pump–probe experiment a polarized detection laser can be used to probe the angular momentum distribution of a polarized atomic product. Over the past few years this has been exploited in great detail [2], especially in combination with the velocity map imaging technique [3], which measures the laser polarization dependent angle-velocity distribution of state-selected products. Up to now, the accuracy of the product angular distribution from imaging experiments has been limited by numerous experimental factors, as discussed in detail in [4]. In this article we describe an experimental system where many of these factors are absent or can be corrected for in order to produce more accurate velocity and angular distributions. One important but complicating variable, the atomic product angular momentum polarization, is in the present case absent because we probe a perfectly spherical atomic <sup>1</sup>S electronic state, arising from the photodissociation of carbonyl sulphide.

Carbonyl sulphide (OCS) is important in atmospheric chemistry and also as a benchmark molecule for photodissociation dynamics [5]. It is highly stable in the atmosphere and can be transported into the stratosphere from the troposphere. Therefore, the photochemistry of OCS in the vacuum ultraviolet (VUV) becomes important because it may be involved in stratospheric ozone chemistry. OCS has a linear structure and belongs to the C<sub>∞v</sub> point group. The ground state OCS ( $\tilde{X}^1\Sigma^+$ ) with (...8σ<sup>2</sup>2π<sup>4</sup>9σ<sup>2</sup>3π<sup>4</sup>) electronic configuration has 16 valence electrons, which is isoelectronic with CO<sub>2</sub> and CS<sub>2</sub> molecules, etc., and their absorption spectra have been reviewed by McGlynn and co-workers [6]. The bond lengths of C–S and C–O are 1.558 Å and 1.165 Å, and the bond dissociation energies of C–S and C–O are 3.12 and 6.81 eV, respectively. The absorption spectrum [6] of OCS consists of three distinct transitions with maxima at ~223.7 nm (<sup>1</sup>Δ ← <sup>1</sup>Σ<sup>+</sup>), ~166.7 nm (<sup>1</sup>Π ← <sup>1</sup>Σ<sup>+</sup>) and ~152.7 nm [7] (<sup>1</sup>Σ<sup>+</sup> ← <sup>1</sup>Σ<sup>+</sup>). At shorter wavelengths are Rydberg-type transitions that have been studied by resonance-enhanced multiphoton ionization (REMPI) [8–10]. Higher superexcited states have been studied in the 12–19 eV region [11–14].

Studies of photodissociation in the 222–249 nm region show that photodissociation takes place via the bent <sup>1</sup>Σ<sup>-</sup> (<sup>1</sup>A'') and <sup>1</sup>Δ (<sup>2</sup>A') states, leading to the

\* Corresponding author. Email: Parker@science.ru.nl

dominant  $S(^1D) + CO(^1\Sigma^+, v=0, \text{high } J)$  channel [15–24].  $S(^1S)$  production from OCS has a large quantum yield in the 142–160 nm regime [25], and raising the temperature increases the yields in the fall-off region (157.7–170 nm) [26]. Photodissociation studies at 157 nm have shown that  $S(^1S) + CO(X^1\Sigma^+)$  is the dominant channel [27, 28]. Strauss *et al.* [28] used laser-induced fluorescence (LIF) to measure both  $S(^1S)$  and  $CO(X^1\Sigma^+)$  products and found the relative vibrational state populations of CO for  $v=0-3$  as (1.0):(1.0):(0.5):(0.3), and a rotational distribution for each vibrational level was found to be near Boltzmann. Similar LIF results have also been reported at 150–155 nm region [29]. Photofragment excitation (PHOFEX) spectroscopy [30, 31] suggested that the  $S(^1S)$  product from 157 nm excitation should arise from a hot band transition from a vibrationally excited level in the electronic ground state  $\tilde{X}^1\Sigma^+$  to the  $2^1\Sigma^+$  excited electronic state.

In this study, atomic sulphur ions ( $S^+$ ) were observed directly from the interaction of OCS with a 157 nm  $F_2$  laser. Significant concentrations of electrons have been observed in photolysis of OCS at 157 nm [32]. The possibility that 157 nm radiation can ionize  $S(^1S)$  through an autoionization process has been suggested previously [33] but not proven experimentally. We investigate this mechanism directly in this paper. Possible mechanisms for  $S^+$  formation are shown in figure 1 and are summarized as follows:

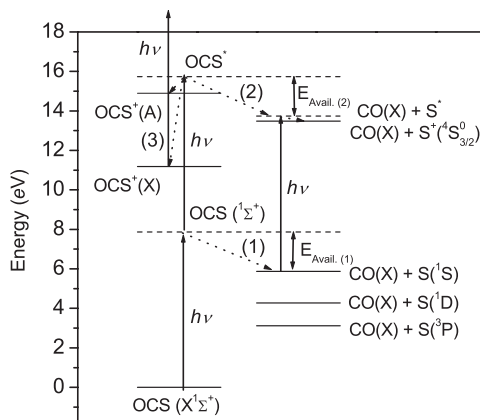
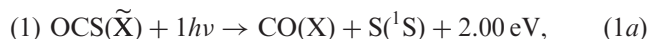


Figure 1. Possible mechanisms of  $S^+$  formation from OCS + 157 nm.

where mechanism (1) is one-photon photodissociation of OCS [28] leading to the predominant  $S(^1S) + CO(X^1\Sigma^+)$  channel (1a), and then the excited state  $S(^1S)$  product absorbs another photon producing  $S^+$  [33]. For mechanism (2), OCS could possibly absorb 2 photons to a repulsive superexcited state ( $\text{OCS}^*$ ) leading to  $S^* + CO(X^1\Sigma^+)$  channel (2a), and the superexcited state product ( $S^*$ ) could then autoionize to produce  $S^+$  (2b) [12, 13]. For mechanism (3),  $\text{OCS}^+$  could be produced by 2-photon excitation (3a) [11, 14], and followed by the photodissociation of the  $\text{OCS}^+$  molecular ion (3b).

## 2. Experimental details

A ‘conventional’ velocity map imaging (VMI) apparatus [3] using a  $F_2$  laser as a light source was applied to study the photochemistry of OCS at 157 nm excitation. Velocity-mapped images of both  $S^+$  ion and electron products were detected after OCS interacted with the 157 nm laser. The images were converted to total kinetic energy release distributions and angular distributions using the Basex [34] inversion program. Recently so-called DC time slicing methods have enlarged the scope of the VMI technique [35, 36]. We have shown that the ‘conventional’ VMI apparatus can also be used for ‘slicing’ [37], and the effectiveness of ‘slicing’ or ‘crushing’ in the present VMI apparatus will be examined in section 3.2.2 and 3.2.3.

### 2.1. Concept

A ‘conventional’ VMI machine consists of a 3-plate annular ion (or electron) aperture lens, which is adjusted to focus charged particles with the same initial velocity vector to the same point in the detection plane [3]. The detection plane is defined here as the  $xy$  plane, the time-of-flight (TOF) axis as the  $z$  axis and the laser propagation direction as the  $x$  axis. Ions which have velocity  $v_x$  and  $v_y$  are focused to  $r_x$  and  $r_y$  in the detection plane, respectively, and  $v_z$  appears in the spread of the ion TOF. Conventionally, a velocity map imaging apparatus is designed to ‘crush’ the entire ion cloud from the 3-dimensional (3D) Newton sphere to a 2-dimensional (2D) detection plane, i.e. projection of signals  $I(v_x, v_y, v_z)$  to  $I(v_x, v_y) = \sum_{v_z} I(v_x, v_y, v_z)$ . The arrival-time spread of product ions from  $-v_z$  to  $v_z$  in an electric field between two parallel plates is determined by the ion turn-around time ( $t_R$ ):

$$t_R = -\frac{2mv_z}{qE_z} = -\frac{2mv_z d}{qV}, \quad (4)$$

where  $m$ ,  $q$  and  $v_z$  are product mass, charge and velocity in the  $z$  direction, respectively;  $d$ ,  $V$  and  $E_z$  are the spacing, voltage and electric field in the  $z$  direction between two parallel plates, respectively. As seen in the equipotential curves for the aperture lenses in the interaction region [3], the electric fields are slightly greater than those for grid-covered parallel plates. Therefore, the  $t_R$  for the lens design should be smaller than that for parallel plates. This will be examined and quantified in section 3.2.3. The mapped position of an ion is given as the following relation:

$$r_x = Nv_x t \approx \left( N' \left( \frac{m}{V} \right)^{1/2} \right) v_x = \left( N' \left( \frac{2}{V} \right)^{1/2} \right) E_{k_x}^{1/2}, \quad (5)$$

where  $N$  is called the magnification factor [3] and has been measured for this apparatus as  $N = 1.34$  from a study of the  $O_2 + 157 \text{ nm} \rightarrow O(^1D) + O(^3P)$  process [37]. TOF ( $t$ ) is estimated to be proportional to  $(m/V)^{1/2}$  for this apparatus. Therefore, the right-hand side of equation (5) is more useful for calibrating the conversion from position to velocity or energy ( $N'$  is a calibration factor and  $E_{k_x}$  is the  $x$  component of the kinetic energy).

For molecular dynamics, the product recoil velocities are distributed on a Newton sphere, and the maxima of  $v_x$ ,  $v_y$  and  $v_z$  on the sphere are the same. Therefore, as we can see in equations (4) and (5),  $V$  is the only parameter that can be practically varied during the experiment and will affect both the arrival-time spread ( $t_R$ ) and the mapped position ( $r_x$  and  $r_y$ ). For the original VMI design [3], the apparatus was implemented for favourable  $r$  and narrow  $t_R$  (normally less than 30 ns) for the ‘crush’ condition. However, the degree of crushing and the possibility of the time slicing is found to be important in our apparatus as described in section 3.2. The DC time-slicing methods [35, 36] modify the conventional VMI by separating the ion turn-around and focusing regions using extra lenses.

## 2.2. Apparatus

A new compact and portable imaging machine was used in this study. This apparatus, based on the original design [3], contains a source chamber and a main detection chamber, which are differentially pumped and separated by a gate valve and a skimmer with a 2 mm diameter aperture.

The main chamber consists of a set of ion (or electron) lenses, field-free TOF region and a ‘position-sensitive’ ion (or electron) detector. The lens consists of 3 plates with 70 mm outer diameter, the so-called repeller (R), extractor (E) and ground (G) plate, with inner diameters of 2, 20 and 20 mm, respectively. Spacings from repeller

to extractor, extractor to ground plate, ground plate to detector are 15, 21.5 and 316 mm, respectively. A ground-shielded TOF tube was used to shield external electric fields. The detector (Burle) consists of dual 40 mm diameter multichannel plates (MCPs) and a phosphor screen (P20), and signals are measured by a charge-coupled device (CCD) camera (Pixelfly). Charged species (ions or electrons) are accelerated and velocity focused onto the detector plane and the desired ion TOF is selected by gating the front MCP with a short high voltage pulse.

The source chamber contains a pulsed solenoid valve (General valve) with a 0.5 mm diameter nozzle and the distance between the nozzle and skimmer is 20 mm. The molecular beam is produced by supersonic expansion and pointed towards the detection plane; the distance between nozzle and interaction region is 80 mm. The source chamber is pumped by a diffusion pump, while the main detection chamber is pumped by a  $1001 \text{ s}^{-1}$  turbo pump. The typical pressure is  $2 \times 10^{-7}$  torr without gas load, and when the valve is running the main chamber pressure is less than  $1 \times 10^{-6}$  torr while the source chamber pressure is less than  $2 \times 10^{-5}$  torr.

## 2.3. Operation

Pure and 1% OCS (Matheson) seeded in Ar was used at 1 atm stagnation pressure. A  $F_2$  laser (PSX-100, MPB) running on a 5 kPa  $F_2$ –He mixture was used in this study and the laser power was  $\sim 0.3 \text{ mJ pulse}^{-1}$ . The laser beam was introduced perpendicular to the molecular beam, i.e. parallel to the detection plane, and the laser was used either unpolarized or polarized by a thin film polarizer (TFP-25012H, LaserOptik). It was applied either unfocused and collimated by a 1 mm diameter iris or focused to the interaction region by a spherical  $CaF_2$  lens with 15.5 mm focal length. A homemade integrated high-voltage power supply and a fast high-voltage pulser were used for the ion lens and detector. Electron images were measured by switching the positive ion–lens voltage to negative electron–lens voltage. The signals were accumulated by a personal computer using DaVis software (LaVision). All the timing was controlled by a two delay/pulse generator (DG535, SRS and BNC 555) at 30 Hz repetition rate. The crush images were inverted using the Gaussian basis set method [34].

## 3. Results and discussion

In this section, sulphur ion ( $S^+$ ) and electron ( $e^-$ ) velocity map images from the interaction of OCS with 157 nm  $F_2$  laser are described first and followed by the

discussion of the photodissociation dynamics. Corrections from ‘imperfect’ to ‘perfect’ images are carried out in order to extract correct anisotropy parameters ( $\beta$ ) and energy distributions. The effects of the image corrections are also compared.

### 3.1. Dynamics of OCS + 157 nm

**3.1.1. S<sup>+</sup> image.** Atomic sulphur ions (S<sup>+</sup>) were detected from the interaction of OCS with the F<sub>2</sub> laser. The S<sup>+</sup> products were observed from both neat and 1% OCS seeded in Ar, using either a focused or unfocused laser. The images were not significantly different using neat or 1% OCS indicating that the S<sup>+</sup> products are from the OCS monomer. There were also no significant difference when using a focused or an unfocused laser, implying that the S<sup>+</sup> products from the 3-photon processes (Mechanism (3)) should not be important. Figure 2 shows the S<sup>+</sup> raw and inverted images and the derived speed distribution. The image shown here is from 1% OCS seeded in Ar using a focused laser because this shows slightly better velocity resolution than the neat OCS beam using an unfocused laser. As we can see from the speed distribution and the assignment, the S<sup>+</sup> signals are well correlated to the OCS + 157 nm → S(<sup>1</sup>S) + CO (X) channel.

**3.1.2. e<sup>-</sup> image and photoion mass spectrum.** The left panel in figure 3 shows the electron image taken using a beam of pure OCS and the 157 nm laser. Only a single channel was observed for the electron products. The crush image shown here was corrected for roundness and background subtracted.

As we can measure from the photoionization TOF mass spectrum, the main peak is at  $m/e = 32$  amu (<sup>32</sup>S<sup>+</sup>), with weak peaks at 34 amu (<sup>34</sup>S<sup>+</sup> isotope) and 60 amu (OCS<sup>+</sup>), and very weak signals at 28 amu

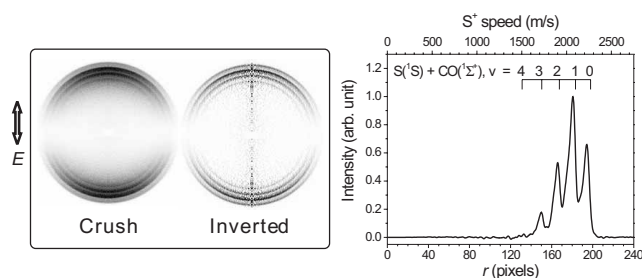


Figure 2. S<sup>+</sup> images and derived speed distribution from the interaction of OCS +  $nh\nu$  (157 nm). The left panel are the raw crush image and its inverted image. The right panel is the derived speed distribution from the inverted image. The assignments above are correlated to the OCS + 157 nm → CO(X) + S(<sup>1</sup>S) channel. Darker regions correspond to larger signals.

(CO<sup>+</sup>), and other minor peaks from the pump oil in the chamber. The CO<sup>+</sup> signals vanished when the OCS concentration was lowered, indicating that the CO<sup>+</sup> might be produced from (OCS)<sub>x</sub> clusters. The electron signals from the pump oil and other scattered light-induced photoelectrons from metal surfaces inside the chamber can be subtracted by setting the laser on and off resonance with the molecular beam in time. Therefore, this photoionization mass spectrometry data shows that the electron signal is correlated to <sup>32</sup>S<sup>+</sup> ions. The right panel in figure 3 is the electron speed distribution derived from the inverted image. Due to the magnetic field penetration of our apparatus, the electron energy uncertainty is large, with a peak at  $0.23 \pm 0.05$  eV.

The angular distribution of photodissociation and photoelectron products is described as the anisotropy parameter ( $\beta$ ) [38]:

$$I(\theta) = \frac{1}{4\pi} [1 + \beta P_2(\cos \theta)], \quad (6)$$

where  $P_2(x)$  is the 2nd Legendre polynomial,  $\theta$  is the angle relative to the polarization axis and  $-1 < \beta < 2$ . The  $\beta$  extracted from the electron image is  $0.61 \pm 0.1$ , based on repeated measurements. In principle, it is possible to predict the electron angular distribution [39, 40], but we have insufficient information to do so at this time.

**3.1.3. Reaction mechanism.** OCS<sup>+</sup> signals with almost zero recoil energy were indeed very weakly detected (equation (3a)). However, the only significant electron signal was seen at  $\sim 0.23 \pm 0.05$  eV and as we can see from the energy level diagram (figure 1), mechanism (3) is definitely not important for S<sup>+</sup> formation. The electron energy is in agreement with equation (1b). Therefore, both S<sup>+</sup> and e<sup>-</sup> results show very good agreement with the mechanism (1).

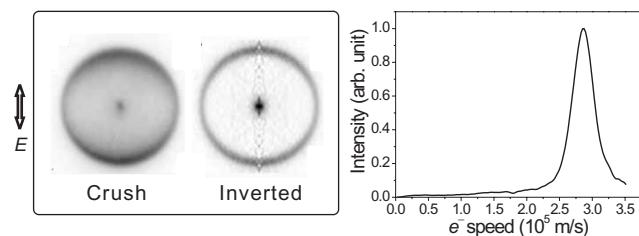


Figure 3. Electron images and derived speed distribution from the interaction of OCS +  $nh\nu$  (157 nm). The left panel are the raw crush image and its inverted image. The right panel is the derived speed distribution from the inverted image. The weak signal observed in the centre of the raw image has an effective volume of zero and thus disappears in the speed distribution.

The lasing lines from the F<sub>2</sub> laser running on a 5 kPa F<sub>2</sub>-He mixture have been precisely measured recently [41], indicating a vacuum wavelength as 82.1% at 157.63094(10) nm, 16.4% at 157.52433(10) nm and 1.5% at 156.73519(10) nm, and the band widths of those lines have been estimated at between 0.62 and 0.82 pm, i.e. 0.25 and 0.33 cm<sup>-1</sup>. The autoionization cross-sections of S(<sup>1</sup>S) at these lines have been estimated as  $1.2 \times 10^{-18}$ ,  $5.0 \times 10^{-18}$  and  $1.1 \times 10^{-18}$  for the transitions at these lines, respectively [33]. Note that direct ionization (a bound-free transition) will ionize all product atom velocity components equally. McGuire [33] has shown that direct ionization of S(<sup>1</sup>S) is improbable ( $\sigma$  is on the order of  $10^{-21}$  cm<sup>2</sup>) at the F<sub>2</sub> laser wavelength. A bound-bound transition to a long-lived autoionizing state directly resonant with one of the F<sub>2</sub> laser wavelengths will ionize only a subcomponent of the 0.45 cm<sup>-1</sup> broad Doppler profile for 2050 m s<sup>-1</sup> S atoms, yielding a vertical stripe (Doppler slice) of the full image. The observed images (after correction for detector inhomogeneity) show no Doppler selectivity, meaning that the autoionization cross-section is essentially constant across the image [33].

The absorption cross-section for jet-cooled OCS at 157 nm is around  $1 \times 10^{-19}$  cm<sup>2</sup> [6, 7]. Photoionization of S(<sup>1</sup>S) has thus a 10–50 times higher cross-section than its production, which suggests that previous LIF detection studies observed only a fraction of the <sup>1</sup>S yield, and this fraction will be strongly wavelength dependent in the 165–150 nm region.

In order to obtain accurate S(<sup>1</sup>S) speed and angular distributions and compare with the previous results [28], a number of image corrections were found to be important and will be described in the following section.

### 3.2. Correction from ‘imperfect’ to ‘perfect’ images

The ion imaging technique has been extensively applied to molecular photodissociation and reaction dynamics in the last few years, mainly due to the high resolution, high detection efficiency, relatively low cost and simple experimental construction. However, several technical aspects of imaging that are normally neglected up to now could be in some cases significant. In this paper we attempt to estimate and quantify most of the latent experimental artefacts and to correct them. The measured raw images could be ‘imperfect’ due to many reasons, including the 3D detection sensitivity function, an imperfect crush or slice due to the ion turn-around time (section 2.1), etc. Correction for imperfect laser polarization will also be described in this section. These factors especially bias the angular anisotropy parameter ( $\beta$ ) and are observed most strongly for lower kinetic

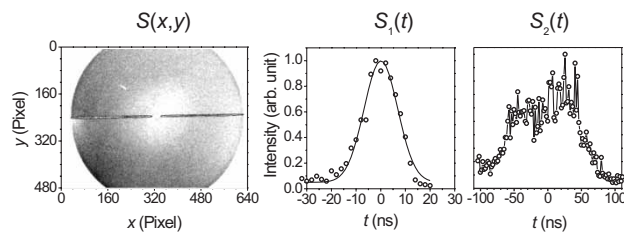


Figure 4. Sensitivity functions of the imaging detector. The left panel is the position-dependent sensitivity function  $S(x, y)$ . Intensity of  $S(x, y)$  from white to dark is from 0.6 to 1. The dark horizontal line is due to a wire for mounting a 2 mm diameter beam stop in front of the detector. The middle panel is the time-dependent sensitivity function  $S_1(t)$  for ‘narrow’ gate averaged over the detector while the right panel  $S_2(t)$  is for the ‘wide’ gate.

energy channels that are overlapped by higher energy channels.

**3.2.1. 3D detection sensitivity correction.** Event counting is usually assumed to remove any spatial variations in gain across the 2D detector. This is not always true, as shown here. Position-sensitive imaging detectors always have an inhomogeneous position sensitivity function, namely  $S(x, y)$ , i.e.  $S(v_x, v_y)$  for velocity map imaging. The inhomogeneity will become worse after some regions have been more often ‘used’. The sensitivity function  $S(x, y)$  can be measured by applying a uniform signal over the entire detector. A simple way to provide a reasonably uniform signal is used here, from the isotropic and fast H<sup>+</sup> background signals coming from the photolysis of pump oil in the chamber. This distribution is flat when using a very small repeller voltage ( $V_R = 200$  V). The measured  $S(v_x, v_y)$  is shown in the left panel in figure 4. The outside form is the outline of the 40 mm diameter detector. As we can see using standard event counting conditions, the sensitivity is indeed not uniform and is especially weaker in the centre region of the detector, which is  $\sim 30\%$  weaker than the outside edge. A raw image ( $I_{\text{raw}}$ ) can be divided by this sensitivity function ( $S$  image) to obtain a corrected image:  $I_{\text{corrected}}(x, y) = I_{\text{raw}}(x, y)/S(x, y)$ .

There is also inhomogeneity of sensitivity in the time domain, namely  $S_i(t)$ , due to the non-uniform gate voltage. This can be measured by scanning the detector-gate through a very narrow signal, for example, scattered photons, electrons, or ions with very small  $v_z$  spread. The limit of the narrowest trigger width for our homemade pulser is set as 50 ns and the sensitivity function  $S_1(t)$  is shown in the middle panel in figure 4. The solid line is the Gaussian fit which shows that the effective detection gate width is as narrow as 14 ns (FWHM). The limitation is mainly due to the rise time of the high-voltage transistor switch. The narrow gate

can be applied to slice the product Newton sphere if the product arrival-time spread in the  $z$  direction is a few times greater than this gate width. For a wider gate width, however, the detection sensitivity is not uniform mainly due to the voltage ‘ringing’ effect that occurs by applying a gated high voltage to the front MCP, and the sensitivity is very nonlinear with the applied voltage. The voltage ringing effect is due to the inductance ( $L$ ) and capacitance ( $C$ ) of the cable and MCP, where ringing frequency is  $f = (1/2\pi)(LC)^{1/2}$ . The ringing high-voltage could be absorbed using a Zener diode with bias that is positioned right before the MCP detector. However, in this study a larger resistor (150  $\Omega$ ) was used to damp the ringing intensity. The best condition was found to trigger this pulser by a 250 ns width. The right panel in figure 4 is the inhomogeneity function  $S_2(t)$ , which shows a  $\sim 100$  ns effective detection gate width. This gate was used to ‘crush’ the entire ion products. In principle, we can use this function  $S_2(t)$ , i.e.  $S(v_z)$  to correct the crush image if we know the correlated arrival time of the product ions. However, due to the complexity, it is more practical to scan the  $S_1(t)$  through the whole ion cloud and sum the resulting images to obtain a perfect crush image.

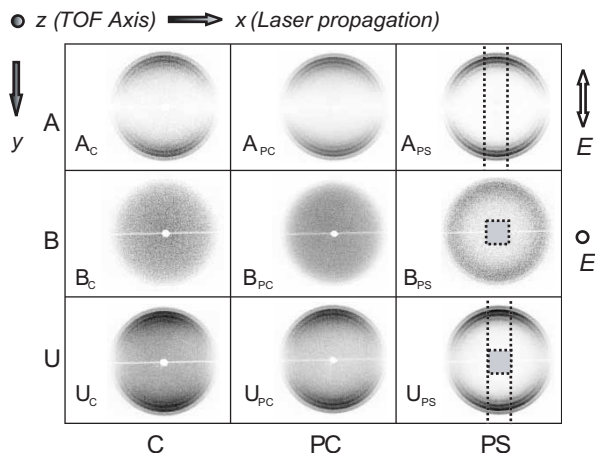


Figure 5.  $S(^1S)$  product images from impurely polarized (A and B) and unpolarized (U) photolysis light using time crush (C), partial-crush (PC) and partial-slice (PS) imaging methods. The laser propagates along the  $x$  axis and the polarization axis is along the  $y$  axis for the A images, while the polarization axis is along the TOF axis ( $z$ ) for the B images. Images labelled as PC are taken using the non-uniform ‘wide’ detector time gate ( $\sim 100$  ns), while images labelled as PS are with the ‘narrow’ gate (14 ns), and images labelled as C are summation of images labelled as PS over the entire ion cloud in the time domain. Background signals have been subtracted and the images are corrected for the position-dependent sensitivity function of the detector,  $S(x, y)$  in figure 4. The dashed-line regions are used to extract the  $\sim 1D$  profiles shown in figure 6.

**3.2.2. Crushing and slicing using conventional imaging apparatus.** Images in figure 5 were taken for different laser polarization geometries with different detector gate widths. Column PC are ‘crush’ images taken using the ‘wide’ gate condition; however, due to the sensitivity function  $S_2(t)$  shown in figure 4, they are imperfect crushes, and here we call them partial crushes (PC). Column PS are slice images taken using a ‘narrow’ gate ( $S_1(t)$  in figure 4) to slice the centre part of the arrival product ions. We call them here partial slices (PS) because the arrival-time spread is not large enough to result in narrow slices by this gate. The perfect crush images (C) as shown in the left panels in figure 5 are taken by scanning the narrow gate through the entire product signals. However, a perfect slicing condition was not reachable in this study due to the limitation of the apparatus (the perfect slice is provided by the inverted image of the perfect crush).

**3.2.3. Turn around time ( $t_R$ ) measurement.** The arrival-time spread of the product ions is determined by the ion turn-round time ( $t_R$ ) described in equation (4) for an ideal electric field between two parallel plates. For this apparatus, the ratio of extractor to repeller voltage ( $V_E/V_R$ ) for velocity map condition is 0.742 and their spacing is  $d = 15$  mm. By substituting these parameters we can obtain

$$t_R = c \frac{mv_z}{V_R} \text{ (ns)}, \quad (7)$$

where the units of  $m$ ,  $v_z$  and  $V_R$  are amu,  $\text{m s}^{-1}$  and volt, respectively, and the factor  $c$  is calculated as 1.21 assuming an ideal parallel-plate field. As we can calculate from the speed distribution in figure 2, the  $S^+$  product mean speed ( $\bar{v}_z$ ) is  $\sim 2050 \text{ m s}^{-1}$ . The mass of  $S^+$  is 32 amu and the repeller voltage used is  $V_R = 1500 \text{ V}$ , and the ion turn-around time can be calculated as  $t_R = 53 \text{ ns}$ .

The arrival-time spread was experimentally measured by scanning the narrow gate through the product ion cloud. Figure 6 shows 1-dimensional (1D) profiles for the products when using an impurely polarized and an unpolarized laser beam. Images  $A_C$  and  $U_C$  in figure 5 are projected from the 3D sphere  $I(v_x, v_y, v_z)$  to the 2D image  $I(v_x, v_y)$ , and are projected to the 1D profile  $I(v_y)$  as shown in the left panels in figure 6. Note that we compare these profiles with the Doppler profiles, which are equivalent measurements but with higher velocity resolution (the lower left panel in figure 6 is equivalent to figure 4 in [28]). The TOF profiles (dashed curves in left panels) are the 3D sphere projected to TOF: in the upper left panel,  $I(t) = \sum_{v_x, v_y} A_{PS}(v_x, v_y)(t)$ , while in the lower left panel,  $I(t) = \sum_{v_x, v_y} U_{PS}(v_x, v_y)(t)$ .

Solid curves in the right panels in figure 6 are the  $\sim 1\text{D}$  velocity profiles taken from the dashed-line regions shown in images  $A_{\text{PS}}$  and  $U_{\text{PS}}$  in figure 5. The dashed curves in the right panels in figure 6 are taken from the grey square regions; in figure 5 are the equivalent regions as for the  $\sim 1\text{D}$  velocity profiles but through the time domain. In the  $\sim 1\text{D}$  profiles, the TOF spread between two peaks are 44 ns, which are correlated to the velocity spread ( $2 \times 2050 \text{ m s}^{-1}$ ). Thus, the velocity and TOF profiles can be normalized and compared together as shown in figure 6. They are in good agreement and the broader TOF profiles are due to the 14 ns gate width.

The measured ion arrival-time spread is the same as the turn-around time ( $t_{\text{R}}$ ) in equation (7). Hence, the turn-around time is measured as  $t_{\text{R}} = 44 \text{ ns}$  and is smaller than the calculated  $t_{\text{R}} = 53 \text{ ns}$  for ideal parallel plates due to the distorted electric field in the  $z$  direction. We can obtain the coefficient in equation (7), yielding  $c = 1.0$  for this apparatus. Equation (7) is thus useful for calculating the arrival-time spread before carrying out an experiment.

**3.2.4. Extraction of the degree of laser polarization from the images.** The extinction ratio ( $T_{\text{p}} : T_{\text{s}}$ ) for the 157 nm TFP (LaserOptik) is ideally greater than 40 in transmission. However, it becomes lower if the TFP surface becomes ‘dirty’. The  $\text{S}(^1\text{S})$  images using different

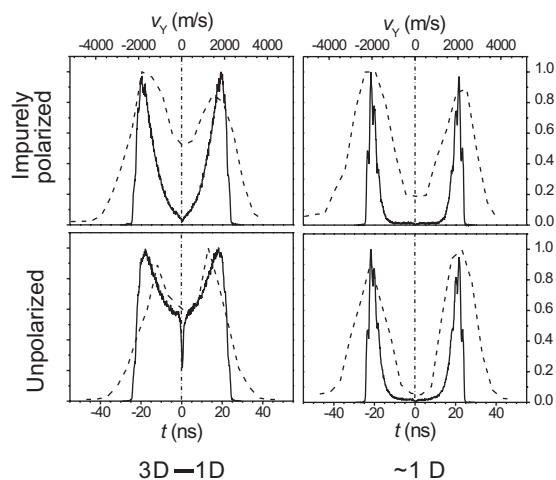


Figure 6. Comparison between TOF profiles (dashed line) and velocity ( $v_y$ ) profiles (solid line). Upper panels are from the impurely polarized laser while lower panels are from the unpolarized laser. Left panels are 1D projections from the 3D Newton spheres ( $3\text{D} \rightarrow 1\text{D}$ ) while right panels approach to direct 1D detection ( $\sim 1\text{D}$ ). The profiles are derived from the images in figure 5 and horizontal scales are normalized to the peak positions (see details in text). The centre glitch in the lower left panel is due to the beam stop and its mounting wire.

polarization geometries can be used to extract the degree of polarization of the photolysis light. The photodissociation angular distribution from unpolarized light can be separated into two linear components having the following relations:

$$\begin{cases} A = a(H + fV), \\ B = b(fH + V), \\ U = \frac{1}{2}(H + V), \end{cases} \quad (8)$$

where  $H$  and  $V$  are images from perfect linear polarized photolysis light in the  $y$  and the  $z$  direction, respectively, and  $f = T_{\text{s}}/T_{\text{p}}$  is the reciprocal of the TFP extinction ratio.

The key to extracting the  $a$ ,  $b$  and  $f$  factors is to use the angular distributions of the  $B$  images in figure 5. It is indeed difficult to see the angular anisotropy directly from the  $B(x, y)$  images. However, it becomes clear if they are transformed to polar coordinates (upper panel in figure 7). The angular anisotropy for the outer rings is shown in the lower panel of figure 7. Because of the large anisotropy of the  $\text{S}(^1\text{S})$  products ( $\beta \sim 2$ ), there are much fewer contributions of isotropic signals from the polarization in the  $z$  direction. Therefore,  $B$  images can be manipulated to yield an isotropic angular distribution, i.e. by making the profile as shown in the lower panel in figure 7 ‘flat’. For crushed images, the relation  $U_{\text{C}} = A_{\text{C}} + B_{\text{C}}$  is fulfilled and the relations,  $B_{\text{C}} - 0.10U_{\text{C}} \propto V_{\text{C}}$  and  $B_{\text{C}} - 0.05A_{\text{C}} \propto V_{\text{C}}$ , were found to produce an isotropic angular distribution ( $\sim V_{\text{C}}$ ). Therefore, the factors are worked out as  $a = b = 0.95$  and  $f = 0.05$ . However, for the partially crushed images, the relations cannot be extracted because the non-uniform time gates were not always in exactly the same position for the ion clouds. For the partially sliced

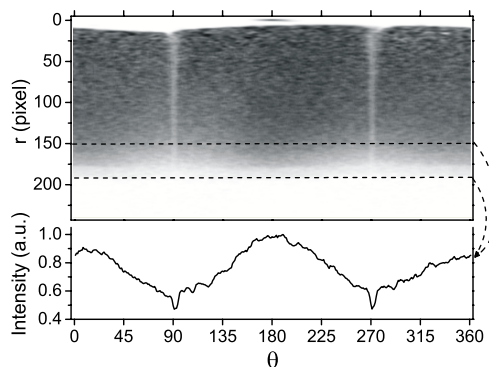


Figure 7. Image  $B_{\text{C}}$  in polar coordinates and angular profile. The image in the upper panel, named  $B'_{\text{C}}(r, \theta)$ , is transformed from  $B_{\text{C}}(x, y)$  in figure 5. The angle  $\theta$  is defined with respect to the  $y$  axis in figure 5. The lower panel is the angular profile averaged between the two dashed lines in the upper panel.

images, the relations  $U_{PS} = 0.79A_{PS} + 0.21B_{PS}$ ,  $B_{PS} - 0.18U_{PS} \propto V_{PS}$  and  $B_{PS} - 0.22A_{PS} \propto V_{PS}$  were found. The factors then can be calculated as  $a = 0.6$ ,  $b = 3.76a = 2.24$  and  $f = 0.06$ . The factor  $f$  is consistent for both measurements as 0.055, i.e. the extinction ratio of the TFP is 18. The degree of polarization of the photolysis source is  $\rho = (I_{\parallel} - I_{\perp}) / (I_{\parallel} + I_{\perp}) = (1 - f) / (1 + f) = 90\%$ . The polarization-corrected images ( $H$ ) are prepared as  $H_C = A_C - 0.05B_C$  and  $H_{PS} = A_{PS} - 0.015B_{PS}$ . It is difficult to provide an accurate  $H_{PC}$  and roughly  $H_{PC} = A_{PC} - 0.1B_{PC}$  was used here.

### 3.2.5. Comparison of ‘perfect’ and ‘imperfect’ images.

Images  $H_C$  and  $U_C$  are called here ‘perfect’ images from polarized and unpolarized photolysis light, respectively. They can be Abel inverted as shown in figure 8. Note that the cylindrical symmetric axis for Abel inversion is the laser polarization direction for polarized photolysis light (upper panels), but becomes the laser propagation direction for unpolarized photolysis light (lower panels). The speed and angular distributions can be derived from these inverted images. The angular distribution of photodissociation products is described in equation (6).  $\theta$  in equation (6) is the angle relative to the polarization axis ( $y$  axis in this paper) for polarized photolysis light. However,  $\theta$  is relative to the laser propagation axis ( $x$  axis in this paper) for unpolarized photolysis light. For polarized photolysis light, a  $\parallel$ -type transition has

$\beta = 2$ , while a  $\perp$ -type transition has  $\beta = -1$  in the limit of fast axial recoil. For unpolarized photolysis light, the  $\parallel$ -type transition has  $\beta = -1$  while the  $\perp$ -type transition has  $\beta = (1/2)$  [38]. It is more convenient to use the following equation for unpolarized photolysis light to obtain a consistent  $\beta$  value comparable to polarized photolysis light:

$$I(\alpha) = \frac{1}{4\pi} \left[ 1 - \frac{1}{2} \beta P_2(\cos \alpha) \right], \quad (9)$$

where  $\alpha$  is the angle relative to the photolysis light propagation direction.

The imperfect images are in principle not Abel invertible due to the lack of a cylindrical symmetry axis. However, they were inverted here to compare the effect of the imperfection. Table 1 contains comparisons of the anisotropy parameters ( $\beta$ ) derived from the perfect and imperfect images. First of all, if the images were not corrected by the detector sensitivity function  $S(x, y)$ , the derived  $\beta$  values (not shown here) fluctuate strongly and yield a bias to higher values ( $\beta > 2$ ), especially for the inner weak ring ( $\nu = 3$ ). For the effects from the depolarization of photolysis light, we can simply see the  $\beta$  values derived from A images (impurely polarized) are consistently lower than those from H images (perfect polarized). They are due to the isotropic components from V images. As we can compare from a non-uniform crush (PC) to uniform crush (C),  $\beta$  values from PC irregularly fluctuate especially for  $\nu = 3$ . For the partially sliced (PS) images, the errors gradually propagate from outer to inner ring from the images. Note that the effect of  $\beta$  values from  $H_{PS}$  increase from outer to inner rings but those from  $U_{PS}$  decrease. This is because for the partial slice the 2D projection of the outer Newton sphere  $I(v_{x_1}, v_{y_1}, v_{z_1})$  is partially summed into the ideal slice  $I(v_{x_1}, v_{y_1}, 0)$ . The trend can be described as we can imagine from the  $H_C$  and  $U_C$  images in figure 8; the unwanted angular distribution of  $I(v_{x_1}, v_{y_1}, v_{z_1} > 0)$  for the partial slice image is more anisotropic for ‘polarized’, and more isotropic for ‘unpolarized’.

Comparing the speed distributions from imperfect to perfect images, the imperfect crush (PC in figure 5) could give positive or negative errors, which are errors propagated from the inversion of the outer ring. The effect is negligible for A (impurely polarized) and H (polarized) images but strong for U (unpolarized) images. This is due to the fact that the signal arrival-time spread for U is broader. The imperfect slicing effects have been described by Shiu *et al.* [42], indicating that in order to obtain a correct branching ratio for two discrete channels, an empirical rule-of-thumb of the slicing ratio ( $t_{\text{slice image}} / t_{\text{full image}}$ ) must be less than  $(1/3)$ .

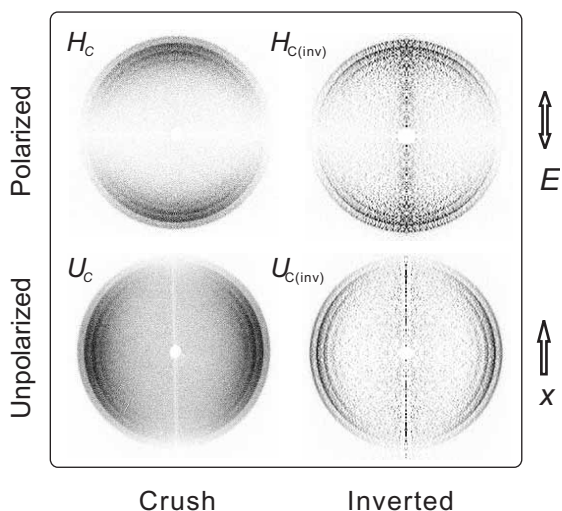


Figure 8. Inversion of images  $H_C$  (upper left) and  $U_C$  (lower left) from polarized and unpolarized photolysis light, respectively. The cylindrical symmetric axis for inversion is along the laser polarization axis ( $y$  or  $E$ ) for  $H_C$  and along the laser propagation axis ( $x$ ) for  $U_C$ . The right panels are their inverted images, namely  $H_{C(\text{inv})}$  and  $U_{C(\text{inv})}$ .

However, this rule cannot be applied to a signal which has a near-continuous distribution. The time slice ( $\sim 1/4$ ) of image (PS) shown in figure 5 is not thin enough to select the centre part of the Newton sphere without the interference from outer Newton sphere signals.

### 3.3. Product internal energy distributions and angular distribution

Figure 9 shows the experimental and simulated product total kinetic energy release distribution. The energy resolution is insufficient to resolve the co-product CO rotational states in the  $S^+$  image. The rotational temperatures for simulation of  $v = 0-3$  are adopted from [28], where  $T_{\text{rot}} = 1350, 1300, 980$  and  $770$ , respectively. Since we can compare the simulated curves with the experimental data, the good agreement supports the near Boltzmann rotational distribution. The relative vibrational state populations for  $v = 0-3$  can be fit as (0.9):(1.0):(0.55):(0.3), which are also close to the previous study, (1.0):(1.0):(0.5):(0.3).

Many factors affect the speed or energy resolution derived from the image [43]. For our apparatus, they might be the rotational and vibrational temperature of the parent OCS molecules, the transverse velocity spread of the molecular beam ( $\Delta v_x$ ), the spread in the photolysis laser ( $F_2$  laser) photon energy, the ion-electron recoil velocity from the ionization scheme, space charge (if the product ion density is too large), velocity-focusing lens aberration, detector resolution, and Abel-inversion and/or noise-induced errors. Each factor must be suppressed in order to rotationally resolve the distribution. This is an ongoing effort in

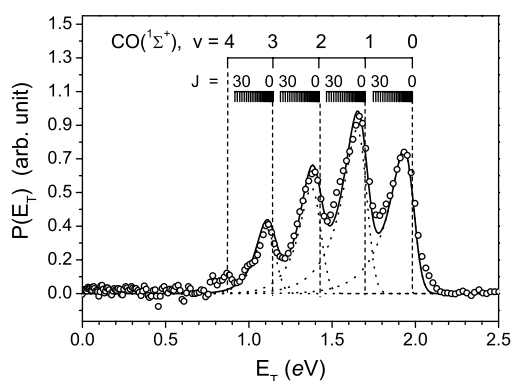


Figure 9. Experimental and simulated product total kinetic energy release distributions of the  $OCS + 157 \text{ nm} \rightarrow S(^1S) + CO(X^1\Sigma^+)$  channel. The open circles are the experimental total kinetic energy distribution, while the dashed curves are simulated distributions correlated to the different vibrational states of CO products and the solid curve is the overall sum of the dashed curves.

our group. Here, we simply use a Gaussian width of  $0.04 \text{ eV}$  for each  $S(^1S) + CO(v, J)$  product channel to simulate the distribution shown in figure 9.

The experimental and simulated distributions show good agreement with the results from Strauss *et al.* [28]. Figure 10 shows the vibrationally resolved angular anisotropy from both a polarized and unpolarized laser. Both show consistent results and the vibrationally averaged  $\beta$  is measured as  $1.96 \pm 0.07$ . The value is slightly higher than the previous LIF study ( $\beta = 1.8 \pm 0.2$ ) [28]. The maximal value of  $\beta = 2$  is approached, confirming a previous conclusion [29] that only a single excited electronic state is involved, i.e. the  $1^1\Sigma^+ - 2^1\Sigma^+$  parallel transition. The observed vibrational distribution (figure 10) is slightly hotter than that of Strauss *et al.* [28] and in accord with the analysis of Itakura *et al.* [29] who showed that energy partitioning into the CO fragment vibration is larger when the  $1^1\Sigma^+ - 2^1\Sigma^+$  transition is excited at  $157 \text{ nm}$ , compared to excitation at the peaks of the continuum at  $152.4, 150.6$  and  $148.9 \text{ nm}$ .

## 4. Conclusion

In this study, we used the velocity map imaging technique to investigate the photochemistry of OCS at  $157 \text{ nm}$ . Atomic sulphur ion products ( $S^+$ ) were observed directly when using a  $157 \text{ nm}$   $F_2$  laser. The results from the  $S^+$  ion image and correlated electron image show that one-photon dissociation of OCS takes place first, leading to the dominant  $S(^1S) + CO(X)$  channel, and the excited atomic sulphur product  $S(^1S)$

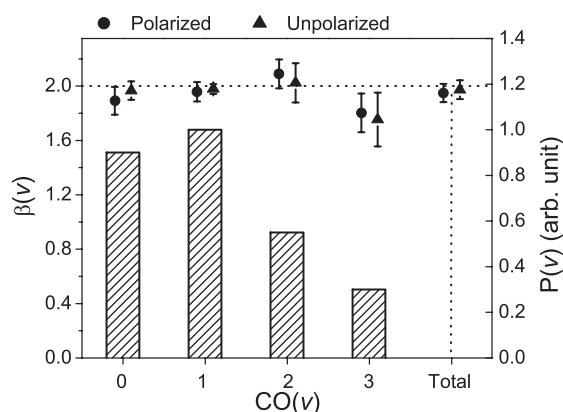


Figure 10. CO product vibrationally resolved  $\beta$  parameters and vibrational distribution. The  $\beta$  values are derived from the 'polarized' and 'unpolarized' data shown in figure 8 (same as rows  $H_C$  and  $U_C$  in table 1, respectively). The bar graph is the relative vibrational distribution from the simulation shown in figure 9.

Table 1. Comparison of vibrational-resolved anisotropy parameters ( $\beta$ ) derived from ‘perfect’ and ‘imperfect’ images.<sup>a</sup> The  $\beta$  values are the weighted average over peaks for different CO vibrational states and the last column is for the entire signal.

Image	CO( $\nu$ )				Total
	0	1	2	3	
$A_C$	1.87(10)	1.93(6)	2.01(9)	1.62(13)	1.90(6)
$A_{PC}$	1.79(24)	1.80(4)	1.87(5)	1.60(8)	1.80(8)
$A_{PS}$	1.79(12)	1.88(3)	1.93(1)	1.91(1)	1.88(4)
$H_C^a$	<b>1.89(10)</b>	<b>1.96(7)</b>	<b>2.09(11)</b>	<b>1.80(14)</b>	<b>1.95(7)</b>
$H_{PC}$	1.82(25)	1.85(5)	2.00(13)	1.96(11)	1.88(10)
$H_{PS}^b$	1.81(12)	1.90(3)	1.97(2)	1.96(1)	1.91(4)
$U_C^a$	<b>1.97(7)</b>	<b>1.98(4)</b>	<b>2.02(14)</b>	<b>1.75(20)</b>	<b>1.97(7)</b>
$U_{PC}$	1.89(12)	1.97(2)	2.03(16)	2.28(48)	1.98(15)
$U_{PS}^b$	1.90(3)	1.84(1)	1.75(2)	1.61(1)	1.79(2)

<sup>a</sup> $H_C$  and  $U_C$  are so-called ‘perfect’ images while the rest are ‘imperfect’ images. See text in details.

<sup>b</sup>The  $\beta$  values from partial slice images are derived directly without Abel inversion.

is ionized by another 157 nm photon. The observed  $S^+$  and  $e^-$  images support the previous study of the  $S(^1S)$  autoionization process [33] and the electron angular anisotropy  $\beta = 0.61 \pm 0.1$  should give rise to further theoretical analysis. During the 157 nm laser pulse the rate of  $S(^1S)$  ionization should largely exceed that of formation, suggesting that caution may be necessary in interpreting LIF detection data. Vibrational resolved angular distributions and energy distributions of the CO products were reported, which show good agreement with a previous study [28], and a more accurate  $\beta$  was measured,  $1.96 \pm 0.07$ .

A procedure to correct the raw velocity map images is also demonstrated here. For the general VMI measurement a number of experimental parameters can affect the angle-velocity distribution, including the detector position-dependent sensitivity function ( $S(x, y)$ ), the Doppler profile, the slicing or crushing effects correlated with the time-dependent sensitivity function ( $S(t)$ ), laser overlap for the two-laser experiment (density-to-flux conversion), aligned products when using polarized laser detection and the purity of the laser polarization. For this study, there are no alignment effects because of the  $^1S$  electronic state and no bias from Doppler effect because of the transition from  $S(^1S)$  to the broad autoionization states. We have shown how to correct for the position-dependent sensitivity function and the purity of laser polarization.

Partial slicing or crushing in ‘conventional’ VMI can be important, and an estimation of the degree of crushing or slicing and the requirements for good slicing or crushing are discussed in this paper.

## Acknowledgements

The authors are grateful to L. Gerristen and P. Claus for their technical support of this study. Thanks are also due to A. M. Coroiu for the contributions to this apparatus and G. Wu for the detector sensitivity-function measurement. XY acknowledges the financial support for his stay in Nijmegen by The Netherlands Organization for Scientific Research (NWO) B66-140. We would also like to thank D. Radenović, A. Eppink and C. Vallence for their helpful suggestions.

## References

- [1] J.P. Simons. *J. phys. Chem.*, **91**, 5378 (1987).
- [2] E.R. Wouters, M. Ahmed, D.S. Peterka, A.S. Bracker, A.G. Suits, O.S. Vasyutinskii. In *Imaging in Chemical Dynamics, ACS Symposium Series 770*, A.G. Suits, R.E. Continetti (Eds), Chapter 15, Oxford University Press, Oxford (2001).
- [3] A.T.J.B. Eppink, D.H. Parker. *Rev. Sci. Instrum.*, **68**, 3477 (1997).
- [4] D.H. Parker, A.T.J.B. Eppink. In *Imaging in Molecular Dynamics, Technology and Applications*, B.J. Whitaker (Ed.), Chapter 2, Cambridge University Press, Cambridge (2003).
- [5] R. Schinke. *Photodissociation Dynamics: Spectroscopy and Fragmentation of Small Polyatomic Molecules*, Cambridge University Press, Cambridge (1995).
- [6] J.W. Rabalais, J.M. McDonald, V. Scherr, S.P. McGlynn. *Chem. Rev.*, **71**, 73 (1971).
- [7] M.I. McCarthy, V. Vaida. *J. phys. Chem.*, **92**, 5875 (1988).
- [8] R. Weinkauff, U. Boesl. *J. chem. Phys.*, **98**, 4459 (1993).
- [9] H. Liu, J. Zhang, S. Ying, D. Xu, B. Jiang, L. Wang, N. Lou. *Phys. Rev. A*, **65**, 052503 (2002).
- [10] R.A. Morgan, A.J. Orr-Ewing, D. Ascenzi, M.N.R. Ashfold, W.J. Buma, C.R. Scheper, C.A. de Lange. *J. chem. Phys.*, **105**, 2141 (1996).
- [11] J. Delwiche, M. Hubin-Franskin, P. Guyon, I. Nenner. *J. chem. Phys.*, **74**, 4219 (1981).
- [12] Y. Hikosaka, H. Hattori, T. Hikida, K. Mitsuke. *J. chem. Phys.*, **107**, 2950 (1997).
- [13] Y. Hikosaka, H. Hattori, K. Mitsuke. *J. chem. Phys.*, **110**, 335 (1999).
- [14] W. Chen, M. Hochlaf, P. Rosmus, G.Z. He, C.Y. Ng. *J. chem. Phys.*, **116**, 5612 (2002).
- [15] N. Sivakumar, G.E. Hall, P.L. Houston, J.W. Hepburn, I. Burak. *J. chem. Phys.*, **88**, 3692 (1988).
- [16] N. Sivakumar, I. Burak, W.Y. Cheung, P.L. Houston, J.W. Hepburn. *J. phys. Chem.*, **89**, 3609 (1985).

- [17] A.J. van den Brom, T.P. Rakitzis, J. van Heyst, T.N. Kitsopoulos, S.R. Jezowski, M.H.M. Janssen. *J. chem. Phys.*, **117**, 4255 (2002).
- [18] A.M. Rijs, E.H.G. Backus, C. A. de Lange, M.M.H. Janssen, N.P.C. Westwood, K. Wang, V. McKoy. *J. chem. Phys.*, **116**, 2776 (2002).
- [19] H. Katayanagi, T. Suzuki. *Chem. Phys. Lett.*, **360**, 104 (2002).
- [20] A. Sugita, M. Mashino, M. Kawasaki, Y. Matsumi, R. Bersohn, G. Trott-Kriegeskorte, K. Gericke. *J. chem. Phys.*, **112**, 7095 (2000).
- [21] Y. Mo, H. Katayanagi, M.C. Heaven, T. Suzuki. *Phys. Rev. Lett.*, **77**, 830 (1996).
- [22] T.P. Rakitzis, P.C. Samartzis, T.N. Kitsopoulos. *Phys. Rev. Lett.*, **87**, 123001 (2001).
- [23] T. Suzuki, H. Katayanagi, S. Nanbu, M. Aoyagi. *J. chem. Phys.*, **109**, 5778 (1998).
- [24] Z.H. Kim, A.J. Alexander, R.N. Zare. *J. phys. Chem. A*, **103**, 10144 (1999).
- [25] G. Black, R.L. Sharpless, T.G. Slinger, D.C. Lorents. *J. chem. Phys.*, **62**, 4274 (1975).
- [26] G. Black, R.L. Sharpless. *J. Chem. Phys.*, **70**, 5567 (1979).
- [27] G.S. Ondrey, S. Kanfer, R. Bersohn. *J. chem. Phys.*, **79**, 179 (1983).
- [28] C.E. Strauss, G.C. McBane, P.L. Houston, I. Burak, J.W. Hepburn. *J. chem. Phys.*, **90**, 5364 (1989).
- [29] R. Itakura, A. Hishikawa, K. Yamanouchi. *J. chem. Phys.*, **113**, 6598 (2000).
- [30] C.D. Pibel, K. Ohde, K. Yamanouchi. *J. chem. Phys.*, **101**, 836 (1994).
- [31] A. Hishikawa, K. Ohde, R. Itakura, S.L. Liu, K. Yamanouchi, K. Yamashita. *J. phys. Chem. A*, **101**, 694 (1997).
- [32] J.K. Rice, J.R. Woodworth. *J. appl. Phys.*, **50**, 4415 (1979).
- [33] E.J. McGuire. *Phys. Rev. A*, **19**, 1978 (1979).
- [34] V. Dribinski, A. Ossadtchi, V.A. Mandelshtam, H. Reisler. *Rev. Sci. Instrum.*, **73**, 2634 (2002).
- [35] J.J. Lin, J.G. Zhou, W.C. Shiu, K.P. Liu. *Rev. Sci. Instrum.*, **74**, 2495 (2003).
- [36] D. Townsend, M.P. Minitti, A.G. Suits. *Rev. Sci. Instrum.*, **74**, 2530 (2003).
- [37] D.A. Chestakov, S.-M. Wu, G. Wu, D.H. Parker, A.T.J.B. Eppink, T.N. Kitsopoulos. *J. phys. Chem. A*, **108**, 8100 (2004).
- [38] R.N. Zare. *Molec. Photochem.*, **4**, 1 (1972).
- [39] J. Cooper, R.N. Zare. *J. chem. Phys.*, **48**, 942 (1968).
- [40] J. Cooper, R.N. Zare. *J. chem. Phys.*, **49**, 4252 (1968).
- [41] C.J. Sansonetti, J. Reader, K. Vogler. *Appl. Opt.*, **40**, 1974 (2001).
- [42] W. Shiu, J.J. Lin, K. Liu, M. Wu, D.H. Parker. *J. chem. Phys.*, **120**, 117 (2004).
- [43] A.T.J.B. Eppink, S.-M. Wu, B.J. Whitaker. In *Imaging in Molecular Dynamics, Technology and Applications*, B.J. Whitaker (Ed.), Chapter 3, Cambridge University Press, Cambridge (2003).